Piezoelectric micromachined ultrasonic transducers with low thermoelastic dissipation and high quality factor

IOP Publishing

Journal of Micromechanics and Microengineering

J. Micromech. Microeng. **28** (2018) 057001 (9pp)

https://doi.org/10.1088/1361-6439/aab1bc

Technical Note

Piezoelectric micromachined ultrasonic transducers with low thermoelastic dissipation and high quality factor

Xuying Chen[1], Xinxin Liu[1], Tao Wang[2], Xianhao Le[1], Fangyi Ma[3], Chengkuo Lee[4] and Jin Xie[1]

[1] The State Key Laboratory of Fluid Power and Mechatronic Systems, Zhejiang University, Hangzhou 310027, People's Republic of China

[2] School of Microelectronics and Solid-State Electronics, University of Electronic Science and Technology of China, Chengdu, People's Republic of China

[3] College of Mechanical and Electrical Engineering, Shaoxing Vocational and Technological College, Shaoxing 312000, People's Republic of China

[4] Department of Electrical and Computer Engineering, National University of Singapore, 4 Engineering Drive 3, Singapore 11757, Singapore

E-mail: xiejin@zju.edu.cn

Received 1 December 2017, revised 7 February 2018
Accepted for publication 23 February 2018
Published 13 March 2018

Abstract

Thermoelastic dissipation is one of the main dissipative mechanisms in piezoelectric micromachined ultrasonic transducers (pMUTs). In this paper, we firstly propose pMUTs with etching holes to decrease thermoelastic dissipation and enhance quality factor (Q). The etching holes effectively disturb heat flow, and thus reduce thermoelastic loss. Working mechanism based on the Zener's model is interpreted. The experiment results show that the Q of pMUT with three rows of holes is increased by 139% from 2050 to 4909 compared with the traditional one. Temperature coefficient of frequency (TCF) and vibration performance are also improved. The enhanced pMUT can be widely used in measurement of Doppler shift and relative high power applications.

Keywords: piezoelectric micromachined ultrasonic transducers, thermoelastic dissipation, quality factor, etching holes

(Some figures may appear in colour only in the online journal)

1. Introduction

Over the past several decades, ultrasound transducers have been developed for applications of non-destructive evaluation [1], medical diagnosis [2], fingerprint identification [3] and so on. Nowadays, conventional bulk piezoelectric ultrasonic transducers and micromachined ultrasonic transducers are commonly used to excite ultrasound. Piezoelectric micromachined ultrasonic transducers (pMUTs) are becoming more and more appealing due to the low acoustic impedance and the convenience for batch production compared with conventional bulk piezoelectric ultrasonic transducers, unnecessary DC polarization voltage and the relatively simple fabrication process compared with capacitive micromachined ultrasonic transducers (cMUTs) [4].

The ultrasonic signal excited by pMUTs has two forms, either a pulse or a continuous wave [5]. The pulse signal normally contains a broad range of frequency to reduce duration for satisfactory axial resolution [6]. Hence the Q of the ultrasonic transmitter is usually very small. The pulse signal

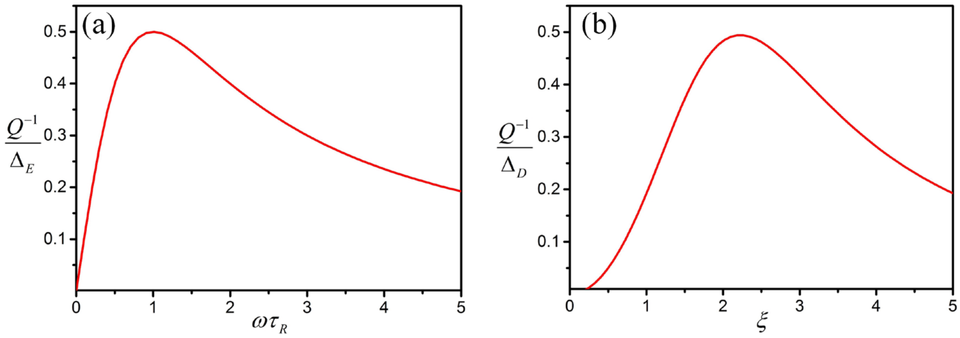

Figure 1. Universal plots of thermoelastic damping based on (a) Zener's theory. (b) Lifshitz's theory.

has been widely used for medical imaging [7], range finding [8] and gesture recognition [9], based on the intensities of waves reflected from various media or time of flight. As for the continuous wave, the transmitting devices are operated at resonance to get efficient excitation and sensitivity. The continuous wave can be used for measurements of Doppler shift in which the frequency band of the continuous wave should be narrow to identify the exact frequency shift, therefore the Q should be as high as possible [5]. Flow meters are one of the applications [10]. High Q continuous-wave ultrasonic transmitters also have advantages in applications of ultrasonic cleaning due to the relatively low power consumption [11].

The main dissipation mechanisms of pMUTs operated at resonance consist of air loss, anchor loss, thermoelastic loss, etc. Air loss caused by the air damping can be minimized by handling the device in vacuum. However, this method is unpractical for pMUTs since the transmission of ultrasound waves requires media. Anchor loss depends on the elastic energy escaping from the vibrating structure through the anchor which connecting it with a frame. The anchor loss can be optimized by locating the anchor at the place where deformation is minimum or reasonably set in-plane acoustic reflectors [12].

Thermoelastic dissipation (TED) is caused by the irreversible heat flow across the temperature gradient which is generated during the elastic deformation in the vibrating membrane. The initial expressions for TED in vibrating structures have been advanced by Zener [13, 14]. In Zener's models, the quality factor determined by thermoelatic dissipation in the direction of flexing beam is,

$$Q^{-1}=\Delta_E\frac{\omega\tau_R}{1+\omega^2\tau_R^2}=\frac{\alpha_T^2TE}{C_p\rho}\frac{\omega\tau_R}{1+\omega^2\tau_R^2} \tag{1}$$

$$\tau_R=\frac{h^2\rho C_v}{\pi^2\kappa} \tag{2}$$

where C_p is the specific heat at constant pressure, C_v is the specific heat at constant volume, ρ is the density of the material, E is the Young's modulus, α_T is the coefficient of linear thermal expansion, T is the temperature of the device, τ_R is the relaxation time, ω is the resonant angle frequency, h is the thickness of the device, κ is the coefficient of thermal conductivity. Zener's models are normally used to calculate the TED in beams, and the Zener curve based on equation (1) is shown in figure 1(a). Another expression has been proposed by Lifshitz *et al* for the TED in beams [15]. Sun and Tohmyoh have modified Lifshitz's expression for applications in out-of-plane vibrating plates [16],

$$Q^{-1}=2\left|\frac{\mathrm{Im}(\omega)}{\mathrm{Re}(\omega)}\right|=\Delta_D\left(\frac{6}{\xi^2}-\frac{6}{\xi^3}\frac{\sinh\xi+\sin\xi}{\cosh\xi+\cos\xi}\right) \tag{3}$$

$$\Delta_D=\frac{(1+\upsilon)\alpha_T\beta T_0}{\rho C_v} \tag{4}$$

$$\xi=h\sqrt{\frac{\omega\rho C_v}{2\kappa}} \tag{5}$$

where υ is the Poisson's ratio, $\beta=E\alpha_T/(1-2\upsilon)$ is the thermal modulus, T_0 is the environmental temperature. The Lifshitz curve based on equation (3) is shown in figure 1(b).

As we can see, the tendencies of Q^{-1} in figures 1(a) and (b) are similar, and the difference is mainly caused by scale factor between the x-axis values which is constant for a given device. The feasibility of Zener's model to analyze the TED of the plates whose vibration modes are similar with pMUTs' has been verified [16]. Lifshitz's theory is often used to account for the effects of geometrical parameters or boundary conditions on TED. In this paper, Zener's model is used to explain the mechanism because the resonant frequency ω and relaxation time τ_R are directly affected by the etching holes.

From equation (1), there are two ways to improve the Q: selecting suitable materials or designing a reasonable structure. Optimizing the geometry design can be attractive. Zhou *et al* have proposed a method to enhance the Q of gyroscopes by hanging lumped mass on the frame structure [17]. Gerrard *et al* have found TED of gyroscopes can be reduced by placing slots to impede the path of heat conduction [18]. Candler *et al* have put forward placing slots at specific locations to improve the Q of resonators [19]. In this paper, we increase the Q of pMUTs by disturbing the irreversible heat flow through etching holes at the boundary of the compressed and tensional region.

2. Method and device

As we can see from Zener's model, Q has the minimum value when $\omega=\nu_R$ (relaxation rate, $1/\tau_R$). It can be understood in this way: if the resonant angle frequency is much smaller than the relaxation rate, the whole system remains in equilibrium called isothermal state and there is little heat flow. Inversely,

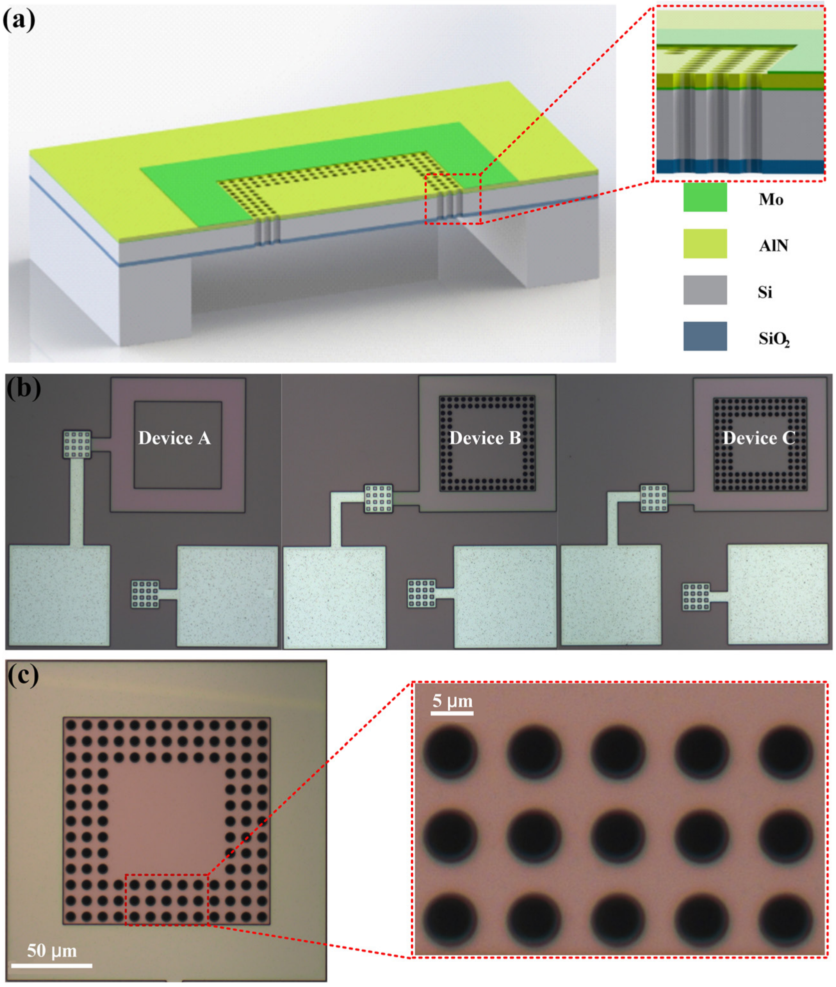

Figure 2. (a) The schematic of the pMUT with three rows of holes. (b) The optical microscope images of the pMUTs, Device A, B, C indicates the traditional pMUT, and pMUTs with two and three rows of holes, respectively. (c) The details of the etching holes.

Table 1. Physical and geometry properties of the silicon devices (298 K) [21].

κ	h	ρ	C_v
$90\ \mathrm{W\ m^{-1}\ K^{-1}}$	$5\ \mu\mathrm{m}$	$2330\ \mathrm{kg\ m^{-3}}$	$1.63 \times 10^6\ \mathrm{J\ (m^3 \cdot K)^{-1}}$

if the resonant angle frequency is much larger than the relaxation rate, the thermal phonons nearly have no time to diffuse and little energy is dissipated i.e. adiabatic process [15]. Therefore, the resonant angle frequency should be far away from the relaxation rate for a high Q.

The schematic view of the pMUT with etching holes is depicted in figure 2(a). The frame-shaped Mo top electrode covers 35% of the AlN piezoelectric layer surface, which ensures effective actuation [20]. Inside the top electrode, holes in diameter of 5 μm are etched through a stack of 1 μm AlN piezoelectric layer, 0.2 μm bottom Mo electrodes, 20 nm AlN seed, 5 μm structure Si and 1 μm SiO_2. Figure 2(b) shows the fabricated pMUTs with and without etching holes. The traditional pMUT without holes is denoted as Device A for reference. Devices B and C indicate the pMUTs with two and three rows of holes, respectively. Figure 2(c) shows the details of the etching holes. Because the main components of the proposed pMUTs are silicon, the relaxation rate of pMUTs can be approximated as that of silicon devices in the same size. The relaxation rate is defined as

$$\nu_R = \frac{1}{\tau_R} = \frac{\pi^2 \kappa}{h^2 \rho C_v}. \tag{6}$$

According to the data in table 1, the relaxation rate of the device is approximately equal to 9.35 kHz. As the resonant frequency of the pMUT is nearly 2.1 MHz, the pMUT obviously works at the adiabatic state. Hence, the larger the resonant angle frequency or the smaller the relaxation rate, the higher the Q.

The etching holes in the membrane of the pMUTs will change part of the heat-transfer material from silicon to air, and the equivalent coefficient of thermal conductivity κ_{equ} is

$$\kappa_{equ} = \frac{\kappa_{si} A_{si} + \kappa_{air} A_{air}}{A_{tot}} \tag{7}$$

where κ_{si} and κ_{air} are the coefficient of thermal conductivity of silicon and air, A_{si} and A_{air} are the heat conduction area through silicon and air, A_{tot} is the total heat conduction area. Because the coefficient of thermal conductivity of air is far less than that of silicon, the equivalent coefficient of thermal conductivity

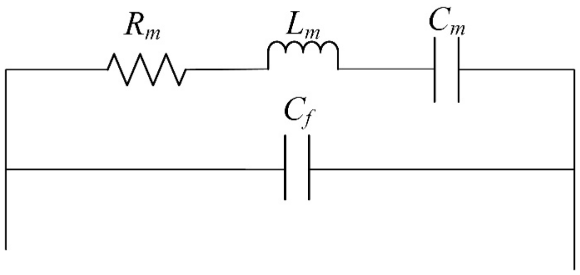

Figure 3. BVD equivalent circuit model for pMUT.

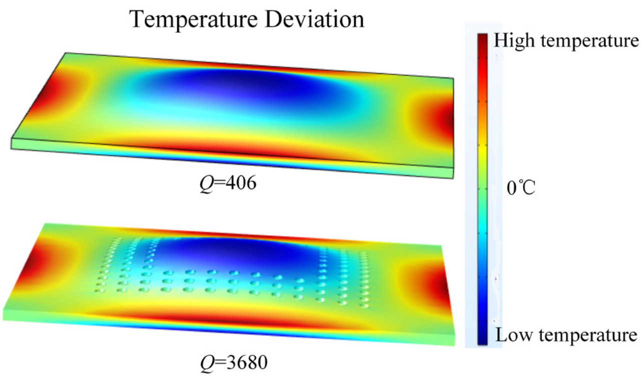

Figure 4. The simulated temperature deviation of the vibrating pMUTs.

κ_{equ} can be greatly decreased. Consequently, the relaxation rate will be decreased. Meanwhile, the etching holes do not affect the resonant frequency of the pMUTs too much, because the conductivity κ_{equ} can be greatly decreased. Consequently, the relaxation rate will be decreased. Meanwhile, the etching holes do not affect the resonant frequency f_0 of the pMUTs too much, because the holes simultaneously reduces the equivalent stiffness k and the equivalent mass m

$$f_0 = \frac{1}{2\pi}\sqrt{\frac{k}{m}}. \tag{8}$$

To sum up, the Q of the pMUTs can be enhanced for the reasons of:

1. The pMUTs work at the adiabatic state;
2. The etching holes can reduce the relaxation rate greatly;
3. The etching holes have little effects on the resonant frequency.

3. Model and simulation

3.1. Equivalent circuit

The Butterworth–Van Dyke (BVD) model is commonly used to represent the pMUTs [22]. The model has four components, R_m, L_m, C_m and C_f, as shown in figure 3. R_m, L_m, C_m are the motional resistance, inductance and capacitance, respectively. The RLC series connection represents the vibration behavior of the pMUTs, which accounts for the series resonant frequency. C_f is the feedthrough capacitance caused by the direct coupling of the top and bottom electrodes, which results in the parallel resonant frequency. The BVD model is used to calculate the exact Q of the pMUTs from the spectral response.

The transfer function of the BVD circuit is described by [23]

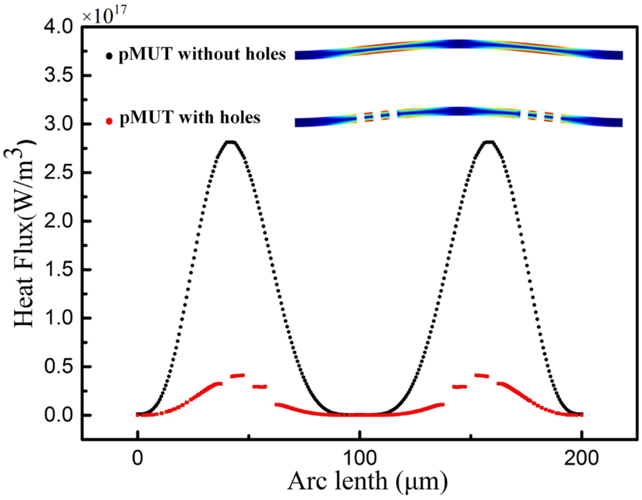

Figure 5. The simulated horizontal heat flux of the vibrating pMUTs.

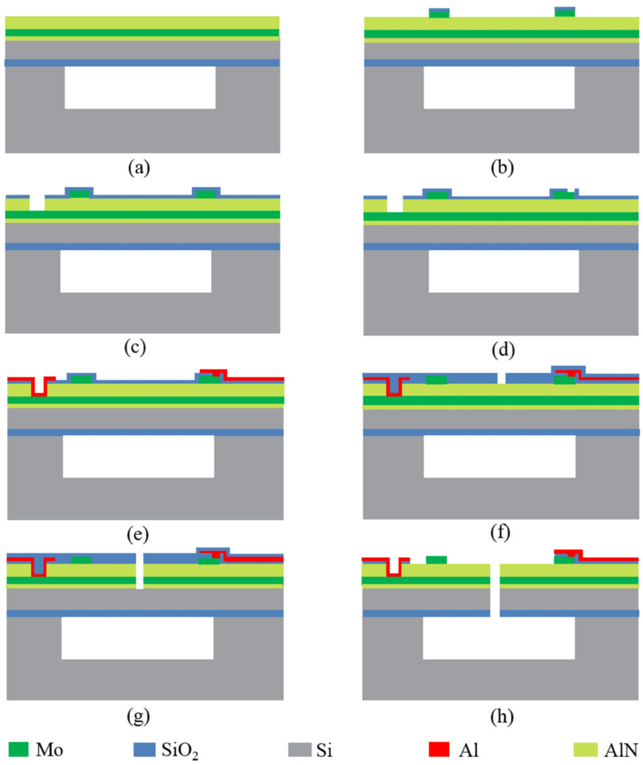

Figure 6. The fabrication process of Device B and C. (a) AlN seed/Mo/AlN deposited. (b) Top electrodes deposited and patterned using SiO_2 as a hard mask. (c) Etching AlN using SiO_2 as a hard mask. (d) Etching SiO_2 using photoresist as mask. (e) Top Al pad deposited and patterned. (f) SiO_2 deposited and patterned. (g) Etching AlN/Mo/AlN to isolate the devices and form holes. (h) Etching Si and SiO_2 to complete the device isolation and holes.

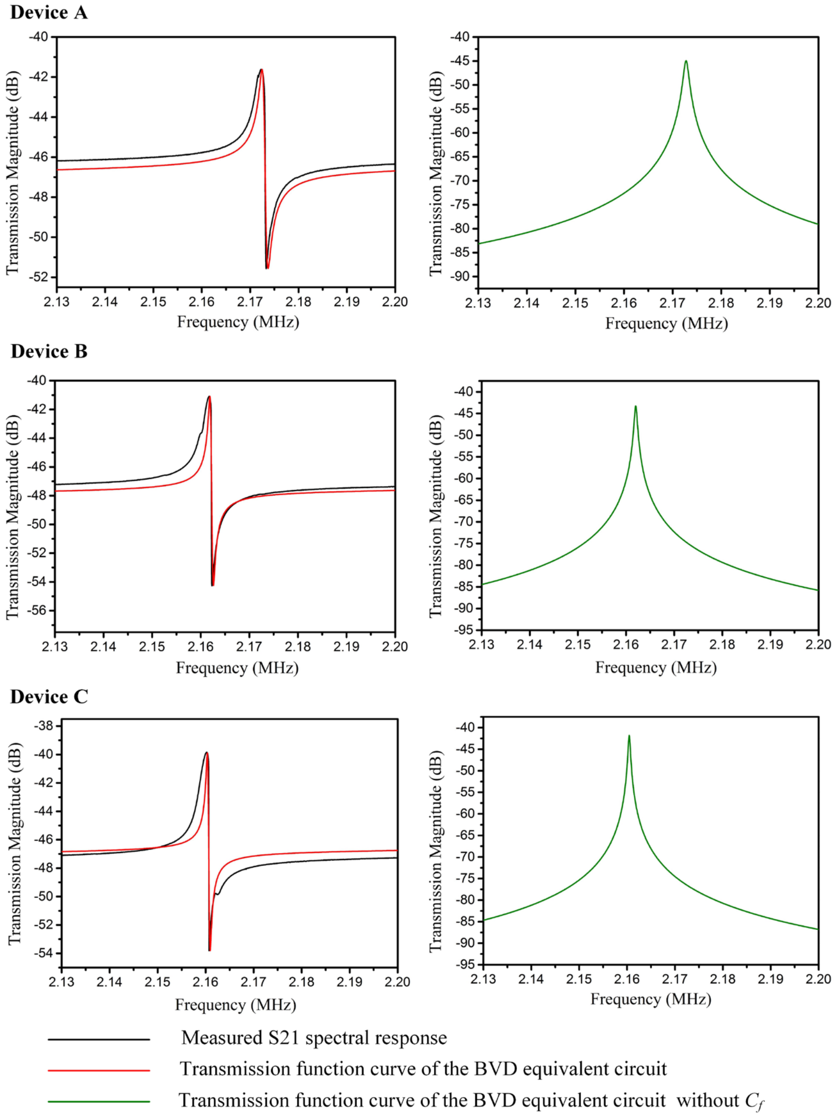

Figure 7. The spectral response of the pMUTs and the transmission function curve of the BVD circuit with or without C_{f}.

$$G(\omega)=\frac{(j\omega)^3C_{\mathrm{f}}+(j\omega)^2\frac{C_{\mathrm{f}}R_m}{L_m}+j\omega\frac{1}{L_m}\left(\frac{C_{\mathrm{f}}}{C_m}+1\right)}{(j\omega)^2+j\omega\frac{R_m}{L_m}+\frac{1}{L_mC_m}}. \tag{9}$$

When the feedthrough capacitance is neglected, the feedthrough signal will be de-embedded, then the pMUTs' parameters can be truly obtained. The transfer function of the circuit without C_{f} is

$$G_{\mathrm{pMUT}}(\omega)=\frac{j\omega\frac{1}{L_m}}{(j\omega)^2+j\omega\frac{R_m}{L_m}+\frac{1}{L_mC_m}}. \tag{10}$$

Given the moderate feedthrough capacitance of pMUTs, a direct parameter extraction method [24] is applied to extract the parameters. The magnitude and frequency associated with the series and parallel resonance peak in the spectral response curve are obtained to calculate the equivalent circuit parameters which satisfy the following equations:

$$f_{\mathrm{s}}=\frac{1}{2\pi\sqrt{L_mC_m}} \tag{11}$$

$$f_{\mathrm{p}}=\frac{1}{2\pi}\sqrt{\frac{C_{\mathrm{f}}+C_m}{C_{\mathrm{f}}L_mC_m}} \tag{12}$$

$$f_0=\frac{(f_{\mathrm{s}}+f_{\mathrm{p}})}{2} \tag{13}$$

$$Q=\frac{\sqrt{L_m/C_m}}{R_m} \tag{14}$$

where f_0 is the resonance frequency; f_{s} and f_{p} are the series and parallel resonance frequency respectively; Q is the quality factor; By comparing the theoretical and experimental spectrum responses which will be shown later, the direct extraction method is verified to be correct.

3.2. Simulation

The temperature deviation of the vibrating pMUTs is simulated by COMSOL multi-physics software. As shown in figure 4, there are two directions of heat flow: vertical and horizontal. Heat flow through the thickness direction is defined as

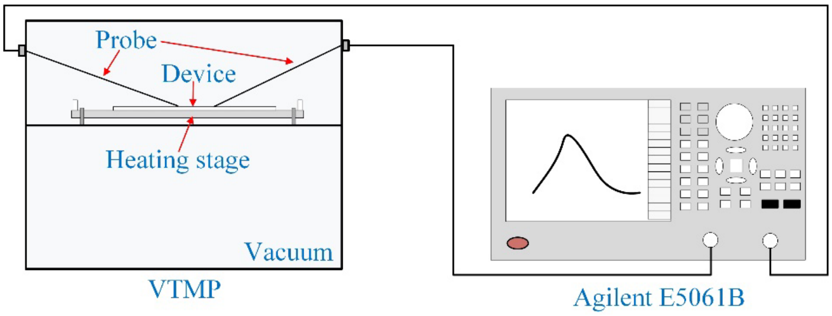

Figure 8. Measurement setup for evaluation of pMUTs' spectral response.

the vertical heat flow, and along the length direction is defined as the horizontal direction. The horizontal heat flow can be reduced by the etching holes, as shown in Devices B and C. The vertical heat flow can be reduced by placing slots inside the membrane, which is difficult for micromachining. The simulated Q can be improved by 9 times because of the etching holes.

The heat flux of Device A and C vibrating at resonance are also compared. The data-collecting-line is set on the center of the top surface. Simulation results in figure 5 show that the heat flux is mainly generated at the boundary of the compressed and tensional region. The etching holes can reduce the horizontal heat flux by nearly 7 times because the etching holes greatly reduce the relaxation rate as previously mentioned, the generated heat flow cannot diffuse rapidly.

4. Fabrication process

All the devices were fabricated at the Institute of Microelectronics (A∗STAR IME) in Singapore. The fabrication process flow is shown in figure 6. It starts from a cavity SOI wafer of 1 μm SiO_2 and 5 μm structural Si. The cavity with a depth of 20 μm defines the location of the pMUT. Then a stack of 20 nm AlN seed/0.2 μm Mo/1 μm AlN is deposited, as shown in figure 6(a). Next, 0.2 μm Mo is deposited and patterned using SiO_2 as a hard mask (figure 6(b)). The top Mo is patterned to define the electrodes ontop of the piezoelectric layer. After a layer of SiO_2 is deposited and patterned on the top electrode, vias are opened to access the top and bottom electrode through etching the AlN (figure 6(c)). And then the oxide is etched again to open the top Mo to top metal vias (figure 6(d)). Subsequently, Al is deposited and patterned to connect the pads with the top and bottom Mo (figure 6(e)). Next, another SiO_2 is deposited and patterned, then the AlN/Mo/AlN stack is etched to isolate the pMUT and form holes (figures 6(f) and (g)). The final step is to complete the pMUT isolation and the holes by etching the Si and SiO_2 (figure 6(h)).

5. Experiment results and discussion

5.1. Quality factor

The spectral response of the pMUTs and the transmission function curve of the BVD circuit with or without C_f are shown in figure 7. The pMUT is tested in a vacuum probe station with temperature control (MMR-K2000), and connected with a network analyzer (Agilent E5061B) as indicated in figure 8. It needs to be emphasized that the extra holes will induce additional air loss. To get rid of the additional air damping, all the Q factors are measured at vacuum level of 0.2 Pa. The etching holes need to be sealed by PDMS [25] in practical applications. Then the similar results can be obtained in the atmosphere.

As we can see, the transmission function curve of the BVD equivalent circuit (Red line) matches the spectral response (Black line) well. The extract parameters of the pMUTs from the spectral response are listed in table 2, C_f, R_m, L_m, C_m and Q are calculated through the formulas mentioned before, Q_s (quality factor of the series resonance frequency) is based on the 3 dB width of the series resonance frequency. The R_m of Device C is the lowest, which is consistent with the lowest damping, therefore the highest Q factor in all of the three devices. The results show that the Q_s is improved by nearly

Table 2. The extracted parameters of the pMUTs.

Parameters	Device A	Device B	Device C
C_f (nF)	34.294	30.405	33.576
R_m (Ω)	176.448	145.142	122.799
L_m (H)	0.027	0.041	0.044
C_m (pF)	20.252	13.137	12.218
f_0 (MHz)	2.173	2.162	2.160
Q_s	527	831	963
Q	2050	3858	4909

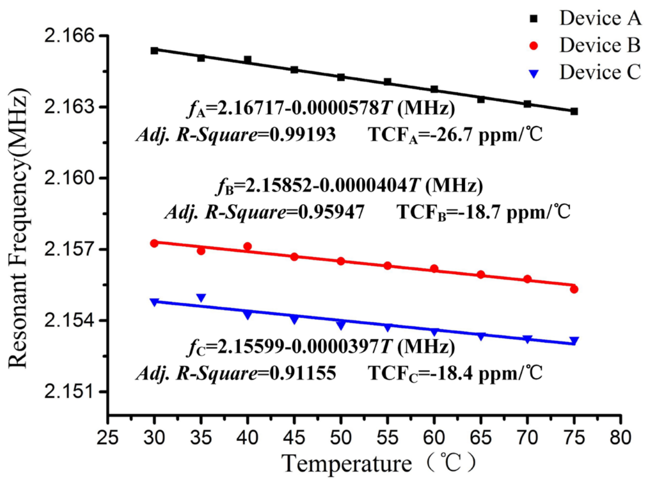

Figure 9. Resonant frequency variations versus temperature of the pMUTs in the atmosphere.

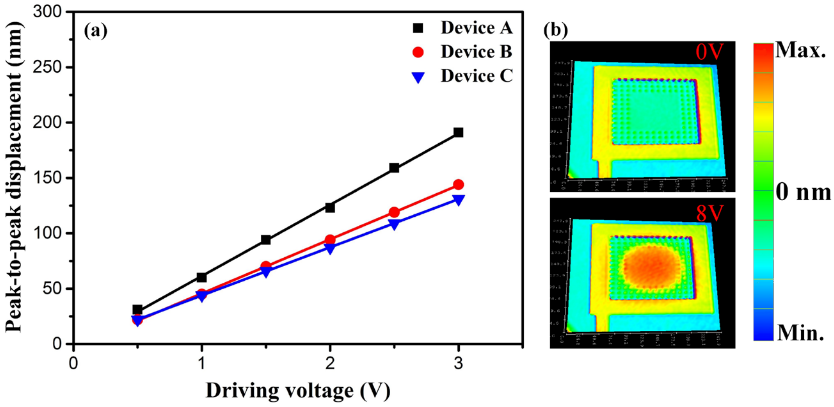

Figure 10. (a) The peak-to-peak displacement of the vibrating membranes at the resonant frequency for different driving voltages; (b) 3D mode shape of Device C.

two times due to the design of etching holes. Similarly the Q of Device C is larger than that of Device A by 139% from 2050 to 4909. Thus, the etching holes are useful to improve the Q of pMUTs. As we have mentioned before, the main loss mechanism of pMUTs contains anchor loss, air loss, and thermoelastic loss. The etching holes are not at proper position of the membrane, so will not optimize anchor loss. Air loss is eliminated at vacuum. As aforementioned, thermoelastic loss can be reduced by the holes according to Zener's model, so the Q is improved mainly due to the reduction in TED. Moreover, the Q of Device C is larger than Device B since the extra row of holes in Device C affects the equivalent coefficient of thermal conductivity more when it is averaged in length.

So far, it has been proved that the etching holes can enhance the Q of pMUTs through optimizing the TED based on Zener's model. Because the classical Fourier thermal conduction theory is applied in Zener's model, the heat flow perpendicular to the surfaces of the beam is ignored. But the Zener's model is still a fair approximation for the analysis because only the horizontal heat flow is considered in this paper.

5.2. Temperature coefficient of frequency

The TCF of the pMUTs is shown in figure 9. TCF is defined as the ratio of the resonant frequency change Δf and the temperature change ΔT over the resonant frequency f_0 [26].

$$\mathrm{TCF} = \frac{1}{f_0}\frac{\Delta f}{\Delta T} = \frac{1}{2}(\mathrm{TCE} + \alpha) \tag{15}$$

where TCE is the temperature coefficient of Young's modulus, and α is linear coefficient of thermal expansion. The variation of Young's modulus E with absolute temperature T is

$$E = E_0 - BT\exp\left(\frac{-T_0}{T}\right) \tag{16}$$

where E_0 is the value of Young's modulus at absolute zero temperature, B is a temperature independent constant related to the bulk modulus, T_0 is a constant related to the Debye temperature.

As we can see, the resonant frequency of the pMUTs has a very good linear relationship with temperature in all the three devices. The TCF of Device A is -26.7 ppm °C^{-1}, while Device B and C have a lower TCF of -18.7 and -18.4 ppm °C^{-1}. Based on the equations (14) and (15), the etching holes may have degenerate effects on parameters α and B, then optimize the TCF. To further decrease the TCF, a passive compensation approach can be employed by using materials with temperature coefficient of modulus opposite to silicon. A pMUT with low TCF is more convenient to excite due to small change of resonant frequency against temperature variation.

5.3. Vibrating characteristic

Vibrating amplitude of the pMUTs is measured by a digital holographic MEMS analyzer (Lyncee Tec. DHM-R2100). The data-collecting-point is located at the center of the membrane, and the data-collecting-line is the diagonal line of the square pMUTs. Figure 10(a) compares the peak-to-peak displacements of the vibrating membranes at the resonant frequency for different driving voltages. The vibrating displacement varies linearly on driving voltage under small input power. The captured 3D mode shape of Device C is shown in figure 10(b). For the pMUT with three rows of holes (Device C) driven at 2 V, nearly the whole membrane inside the electrode moves up just like a piston, as shown in figure 11(b). (Because the depth of etching holes is beyond the measurement range of the analyzer, the offset parameter of the Device C is modified to ensure the continuity of the curve. As a result, the central region inside the electrode is higher than the outside part, and there are two small protrusions in the curve.) This is because the etching holes soften the structure, which can keep the membrane flat during vibration. In comparison, for the pMUT without holes (Device A) driven at 2 V, only the central part of the membrane moves up, which results in a Gaussian-like mode shape, as shown in figure 11(a). Although the displacement of pMUTs with holes is slightly smaller than that of pMUTs without holes, a flat vibrating membrane can generate higher acoustic pressure [27] as indicated in figure 12. The far field space pressure level (SPL) of Device C is 5.3 dB higher than Device A. It is mainly benefited from the piston-like mode shape that a larger portion of membrane vibrates with the maximum amplitude, then more acoustic medium can be pushed out, hence higher ultrasonic pressure is generated. Future work will be sealing the holes by PDMS or Parylene and measuring the specific SPL.

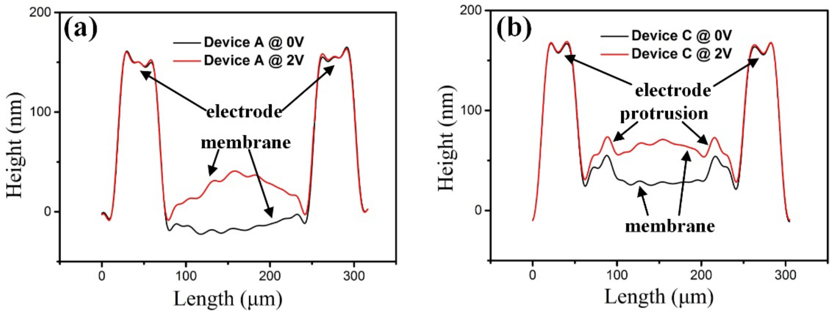

Figure 11. (a) Surface profiles of Device A at resonance; (b) surface profiles of Device C at resonance.

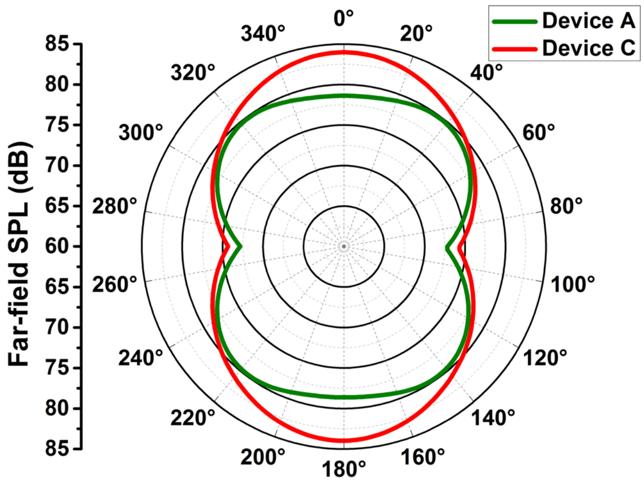

Figure 12. Simulated far field SPLs for Device A and C.

Although the introduction of a polymer will offset part of the improvement in Q, a protective layer which can seal the holes at the same time is essential to prevent short circuit, corrosion, contamination and etc [25]. So the pMUTs with holes still have higher Q than that those without holes in applications. A thinner protective layer will cause less offset [28].

6. Conclusion

In summary, we propose a high-Q pMUT with optimized thermoelastic dissipation (TED) through the etching holes. The working mechanisms based on Zener's model are explained: the etching holes have little effect on the resonant frequency but can reduce the relaxation rate greatly. Simulation and experiment results both verify the effectiveness. The pMUT with three rows of holes has quality factor larger than the traditional one without etching holes by 139% from 2050 to 4909, and slightly larger than the pMUT with two rows of holes. The temperature coefficient of frequency and vibration performance are also improved. The enhanced pMUT has advantages in continuous-wave applications such as measurement of Doppler shift and some relative high power applications.

Acknowledgment

This work is supported by the 'National Natural Science Foundation of China (51475423)', the 'Science Fund for Creative Research Groups of National Natural Science Foundation of China (51521064)' and the 'Fundamental Research Funds for the Central Universities'.

ORCID iDs

Chengkuo Lee https://orcid.org/0000-0002-8886-3649
Jin Xie https://orcid.org/0000-0003-3942-3046

References

[1] Drinkwater B W and Wilcox P D 2006 Ultrasonic arrays for non-destructive evaluation: a review *NDT & E Int.* **39** 525–41

[2] Chen J 2010 Capacitive micromachined ultrasonic transducer arrays for minimally invasive medical ultrasound *J. Micromech. Microeng.* **20** 23001

[3] Przybyla R J, Tang H Y, Shelton S E, Horsley D A and Boser B E 2014 12.1 3D ultrasonic gesture recognition *Digest of Technical Paper—IEEE Int. Solid-State Circuits Conf.* vol 57 pp 210–1

[4] Jung J, Kim S, Lee W and Choi H 2013 Fabrication of a two-dimensional piezoelectric micromachined ultrasonic transducer array using a top-crossover-to-bottom structure and metal bridge connections *J. Micromech. Microeng.* **23** 125037

[5] Muralt P and Baborowski J 2004 Micromachined ultrasonic transducers and acoustic sensors based on piezoelectric thin films *J. Electroceram.* **12** 101–8

[6] Wang T, Kobayashi T and Lee C 2015 Bandwidth micromachined piezoelectric ultrasonic transducer with ultra-wide frequency bandwidth *Appl. Phys. Lett.* **13501** 106

[7] Lu Y, Heidari A, Shelton S, Guedes A and Horsley D A 2014 High frequency piezoelectric micromachined ultrasonic transducer array for intravascular ultrasound imaging *2014 IEEE 27th Int. Conf. Microelectromechanical Systems* pp 745–8

[8] Przybyla R J, Tang H, Member S, Guedes A, Shelton S E, Horsley D A and Boser B E 2015 3D ultrasonic range finder on a chip *IEEE J. Solid-State Circuits* **50** 320–34

[9] Lu Y, Tang H, Fung S, Wang Q, Tsai J M, Daneman M, Boser B E and Horsley D A 2015 Ultrasonic fingerprint sensor using a piezoelectric micromachined ultrasonic transducer array integrated with complementary metal oxide semiconductor electronics *Appl. Phys. Lett.* **263503** 1–5

[10] Van Neer P L M J, Robers T and Volker A W F 2013 A pMUT based flowmeter: a feasibility study *IEEE Int. Ultrasoncs Symp. IUS* pp 1319–22

[11] Potter G, Tokranova N, Rastegar A and Castracane J 2016 Microelectronic engineering design, fabrication, and testing of surface acoustic wave devices for semiconductor cleaning applications *Microelectron. Eng.* **162** 100–4
[12] Harrington B P and Abdolvand R 2011 In-plane acoustic reflectors for reducing effective anchor loss in lateral-extensional MEMS resonators *J. Micromech. Microeng.* **21** 085021
[13] Zener C 1937 Internal friction in solids. I. Theory of internal friction in reeds *Phys. Rev.* **32** 230
[14] Zener C 1938 Internal friction in solids II. General theory of thermoelastic internal friction *Phys. Rev.* **53** 90
[15] Lifshitz R and Roukes M L 2000 Thermoelastic damping in micro- and nanomechanical systems *Phys. Rev.* B **61** 5600–9
[16] Sun Y and Tohmyoh H 2009 Thermoelastic damping of the axisymmetric vibration of circular plate resonators *J. Sound Vib.* **319** 392–405
[17] Zhou X, Xiao D, Hou Z, Li Q and Ted Q 2017 Thermoelastic quality-factor enhanced disk resonator gyroscope micro electro mechanical systems *IEEE 30th Int. Conf. on (MEMS) 2017* (IEEE) pp 1009–12
[18] Gerrard D D, Rodriguez J, Ortiz L C, Chandorkar S A, Flader I B, Chen Y, Shin D D and Kenny T W 2017 Manipulation of heat flux paths in thermo-elastically damped resonators for *Q* optimization *IEEE 30th Int. Conf. on Micro Electro Mechanical Systems (MEMS) 2017* (IEEE) pp 1130–3
[19] Candler R N *et al* 2006 Impact of geometry on thermoelastic dissipation in micromechanical resonant beams *J. Microelectromech. Syst.* **15** 927–34
[20] Muralt P, Ledermann N, Paborowski J, Barzegar A, Gentil S, Belgacem B, Petitgrand S, Bosseboeuf A and Setter N 2005 Piezoelectric micromachined ultrasonic transducers based on PZT thin films *IEEE Trans. Ultrason. Ferroelectr. Freq. Control* **52** 2276–88
[21] Li P, Fang Y and Hu R 2012 Thermoelastic damping in rectangular and circular microplate resonators *J. Sound Vib.* **331** 721–33
[22] Choi H S, Ding J L, Bandyopadhyay A, Anderson M J and Bose S 2008 Characterization and modeling of a piezoelectric micromachined ultrasonic transducer with a very large length/width aspect ratio *J. Micromech. Microeng.* **18** 25037
[23] Ding H, Le X and Xie J 2017 A MEMS fishbone-shaped electrostatic double-ended tuning fork resonator with selectable higher modes *J. Microelectromech. Syst.* **26** 793–801
[24] Lee J E Y and Seshia A A 2010 Direct parameter extraction in capacitively transduced micromechanical resonators using the anti-resonance *2010 IEEE Int. Frequency Control Symp. FCS 2010* pp 133–6
[25] Lu Y and Horsley D A 2015 Modeling, fabrication, and characterization of piezoelectric micromachined ultrasonic transducer arrays based on cavity SOI wafers *J. Microelectromech. Syst.* **24** 1142–9
[26] Boyd E J, Li L, Blue R and Uttamchandani D 2013 Measurement of the temperature coefficient of Young's modulus of single crystal silicon and 3C silicon carbide below 273 K using micro-cantilevers *Sensors Actuators* A **198** 75–80
[27] Guedes A, Shelton S, Przybyla R, Izyumin I, Boser B and Horsley D A 2011 Aluminum nitride pMUT based on a flexurally-suspended membrane *2011 16th Int. Solid-State Sensors, Actuators Microsystems Conf. TRANSDUCERS'11* pp 2062–5
[28] Lu Y, Heidari A and Horsley D A 2015 A high fill-factor annular array of high frequency piezoelectric micromachined ultrasonic transducers *J. Microelectromech. Syst.* **24** 904–13